LOSS OF ALPHA-LIKE MeV FUSION PRODUCTS FROM TFTR

S.J. ZWEBEN, R.L. BOIVIN, M. DIESSO, S. HAYES,
H.W. HENDEL, H. PARK, J.D. STRACHAN
Princeton Plasma Physics Laboratory,
Princeton University,
Princeton, New Jersey,
United States of America

ABSTRACT. A detailed comparison between the observed and expected loss of alpha-like MeV fusion products in TFTR is presented. The D–D fusion products (mainly the 1 MeV triton) were measured with a 2-D imaging scintillation detector. The expected first-orbit loss was calculated with a simple Lorentz orbit code. In almost all cases the measured loss was consistent with the expected first-orbit loss model. Exceptions are noted for small major radius plasmas and during strong MHD activity.

1. INTRODUCTION

Good alpha particle confinement will be necessary to obtain D–T ignition in a tokamak, and accurate predictions of alpha losses will be needed for designing a fusion reactor first wall. This paper describes some recent experiments on TFTR which test our understanding of the 'single-particle' energetic ion confinement obtained with the relatively small populations of D–D fusion products. This understanding can form a baseline for future study of the 'collective' alpha instability and heating effects to be obtained with the ≈ 1000 times larger MeV ion populations expected for ignited D–T plasmas.

1.1. Alpha confinement models

The simplest axisymmetric, neoclassical, alpha particle confinement model predicts that (amost) all alphas which are confined on their first orbit will stay confined until they are thermalized, since energy drag dominates pitch angle scattering during the thermalization process [1, 2]. Thus, alpha loss should become significant when the typical banana width Δ becomes comparable to or larger than about half the minor radius, or roughly:

$$\Delta \approx q(R/a)^{1/2} \rho_{tor} > a/2 \qquad (1)$$

where q is the magnetic safety factor, R is the plasma major radius, a is the plasma minor radius and ρ_{tor} is the toroidal gyroradius. Therefore, the main determinant of alpha confinement at a given toroidal field and aspect ratio (R/a) is the plasma current I, which determines q. Thus, for 3.5 MeV alpha particles in TFTR with R = 245 cm, a = 80 cm, B_{tor} = 50 kG and ρ_{tor} = 5 cm, condition (1) occurs at about I = 1.5 MA. Therefore, first-orbit loss of alpha-like ions should be dominant below about 0.5 MA and negligible above about 2 MA, as has been calculated previously in slightly different forms [1–5].

In fact, at the very highest currents typical of current designs for ignition tokamaks (>10 MA), the neoclassical axisymmetric alpha loss is negligible, and the dominant loss should be due to the small non-axisymmetric toroidal field (TF) ripple, which can cause up to 10–20% of the alpha heating power to be lost to the walls [6–8]. This TF ripple loss is due to relatively slow diffusion of trapped ion orbits and so should occur primarily at the point where the previously confined orbits first intersect the wall, i.e. near the outer equatorial plane [9].

These calculations of axisymmetric and TF ripple losses are fairly straightforward, since they are based on well known vacuum magnetic field configurations. However, more recent models which calculate the loss due to *internally* generated non-axisymmetric perturbations resulting from magnetohydrodynamic (MHD) instabilities or small scale turbulence [10, 11] cannot yet be applied with such confidence, since the magnitudes and the internal structure of these perturbations are not (and may never be) well known. Therefore, it seems appropriate to evaluate the alpha confinement experimentally.

1.2. Previous experimental work

Experimental tests of single-particle alpha confinement can be made by exploiting the similarity between

the 3.5 MeV D–T alphas and two of the charged fusion products routinely created in D–D plasmas, namely the 1 MeV triton and the 3 MeV proton. These two fusion products are similar to the 3.5 MeV alphas with respect to their gyroradii (to within 10%) and thermalization time ($\simeq 0.5$ s), so that their confinement and thermalization physics should be the same for almost any type of fusion product loss mechanism.

Two complementary experimental techniques have been used previously to measure alpha-like D–D fusion reaction products. The first is the 'burnup' technique for *confined* triton detection, which measures the total confined triton population versus time through the 14 MeV neutrons created by the thermalizing tritons in their reactions with the deuterium background plasma. The other technique, used in this paper, is direct measurement of charged fusion product losses to the wall.

Pioneering work on triton (and ^{3}He) burnup in PLT and PBX [12] showed that in many cases the results were consistent with classical confinement and thermalization (to within a factor of three uncertainty), but in some other cases there was an anomalously low burnup at low TF, possibly associated with large MHD activity. Enhanced MeV ion losses associated with MHD 'fishbone' activity were also observed on PBX [13]. More recently, triton burnup measurements on FT [14] and on JET at plasma currents up to 5 MA [15] have shown that global triton confinement and slowing down are *almost always* consistent with the axisymmetric neoclassical model predictions, with possible exceptions being associated with increased MHD activity. Similar TFTR experiments have usually shown a burnup which is anomalously low by a factor of two [16], particularly when the triton slowing down time is long in 'supershots'. Identification of possible anomalous loss mechanisms via the burnup technique tends to be difficult, since the 14 MeV neutron measurements are volume averaged and have relatively poor time resolution (≈ 50 ms).

The complementary technique described in this paper directly measures the loss of charged fusion products to detectors located inside the vacuum vessel but outside the plasma boundary. This method can provide very localized space and time resolved measurements of the triton or proton losses (< 1 cm, < 10 μs), but global triton confinement cannot easily be evaluated, since an integration of these losses over the whole wall area would be necessary.

Direct measurements of D–D fusion product losses were first made in low current tokamaks such as PLT [17, 18] and ASDEX [19]. These experiments measured escaping 3 MeV protons with silicon surface barrier (SSB) detectors in order to determine the deuterium ion temperature, which required good energy resolution but little or no pitch angle resolution.

Other previous measurements have detected the fusion products from D–^{3}He reactions, namely the 15 MeV protons and the 3.7 MeV alpha particles. Particularly relevant to the present experiment was a measurement of the energy and pitch angle distributions of escaping 3.7 MeV alpha particles in PLT [20], which was made with a time integrating plastic track detector in a geometrical configuration similar to the one used here. In TFTR, measurements of the escaping 15 MeV protons from the burnup of the 0.8 MeV ^{3}He ions produced by D–D reactions were made using an array of SSB detectors, with results approximately consistent with neoclassical predictions [21]. In JET, measurements of the 15 MeV protons from ICRF induced D–^{3}He reactions were made using a single-channel SSB detector, with striking results showing large bursts of lost protons associated with sawteeth during ICRF minority heating [22].

Conspicuously absent from the previous experimental work are direct measurements of alpha-like particle losses in the plasma current range 0.5–2.5 MA over which the first-orbit loss should vary from dominant to negligible. Also absent are direct measurements of the enhanced loss which were sometimes observed indirectly through anomalously low triton burnup.

The TFTR work in these directions began with a survey of possible alpha physics experiments [23], and with a prototype, four-channel ZnS scintillation detector [24]. A second 2-D imaging prototype for measuring escaping triton was operated on TFTR in 1987 [25]. That detector, despite its relatively poor time resolution and large soft X-ray background, did demonstrate some of the basic features of triton loss which are reproduced and extended in the present experiment.

The 2-D imaging detection system is described in Section 2 and the experimental results are presented in Section 3. The conclusions, including some tentative theoretical interpretations and directions for further experiments, are listed in Section 4.

2. DETECTION SYSTEM

This section describes the design and operation of the lost triton/proton detection system on TFTR. Many of the general design considerations are similar to those discussed previously for the 2-D prototype detector [25].

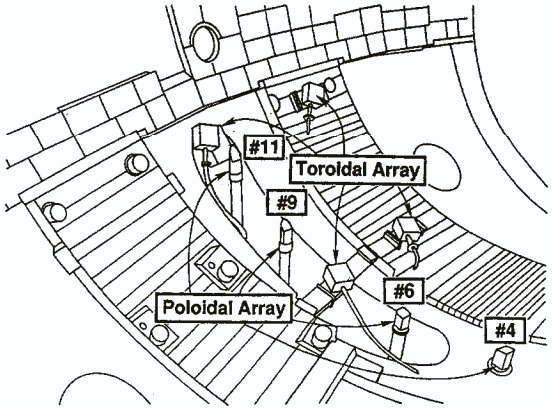

FIG. 1. Location of escaping triton/proton detectors in TFTR during the 1988 run period. Most of the data were obtained from detector No. 6, located at R = 259 cm, approximately 90° below the outer equator. Some data were also obtained from detectors No. 6 and No. 11, located ≈60° and ≈45° below the outer equator, respectively.

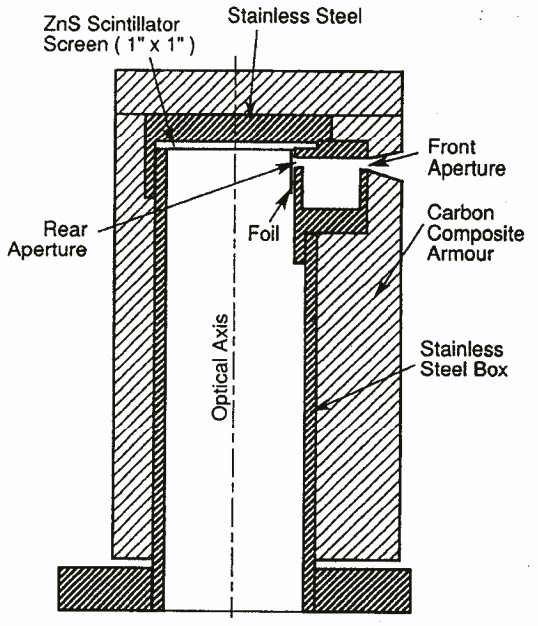

FIG. 2. Mechanical design of detector No. 6. The top of this light-tight detector box is located 2 cm behind the ICRF limiter radius of 99 cm. The front aperture is 0.1 cm high vertically and 0.2 cm wide, the rear aperture is 0.1 cm high and 1.5 cm wide, the aperture spacing is 1 cm, the distance between the aperture centre and the scintillator centre is 1.5 cm, and the vertical distance between the aperture centre and the scintillator plane is 0.2 cm. A thin foil is also located behind the rear aperture to block plasma light. Detectors No. 9 and No. 11 are similar in design, except that the box tops are tilted to be parallel to the local flux surfaces.

2.1. Detector configuration

Figure 1 shows the arrangement of the lost triton/proton detectors inside the TFTR vacuum vessel for the 1988 run. Eight detectors were installed, four of which were inserted from underneath the vessel along a poloidal arc (the 'poloidal array') and the other four were mounted inside the vessel in a square array (the 'toroidal array'). All were fixed in position at the bottom of the vessel (the direction of the ion grad-B drift) during the entire 1988 run.

The experimental results described in Section 3 come almost entirely from detector No. 6, which was located about 90° below the outer midplane (as was the prototype in Ref. [25]). This detector was monitored most carefully because it had the largest signal levels owing to its relatively high optical efficiency. However, the results from the other triton/proton poloidal detectors (Nos 9 and 11) were at least qualitatively similar, as discussed in Section 3.12.

2.2. General detector design

As shown in Figs 2 and 3, the tritons and/or protons enter a pinhole/slit aperture pair, pass through a thin aluminium foil, and then hit a scintillator screen mounted inside the light-tight detector box. The 2-D images of light from the scintillator screen are coupled out of the vacuum system by a relay lens and into an 8 m long

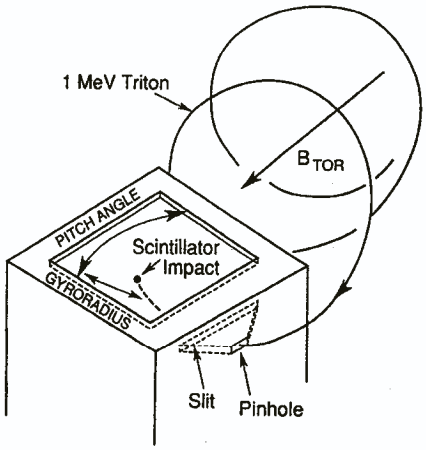

FIG. 3. Functional design of the triton detectors. Tritons with an energy of 1 MeV and a gyroradius of ≈5 cm are incident on helical orbits. These orbits must pass through the front aperture 'pinhole' and the rear aperture 'slit' in order to reach the scintillator. Tritons are dispersed according to their pitch angles and gyroradii in the directions shown.

coherent fibre bundle which runs to signal monitors in the neutron shielded TFTR basement.

Detector No. 6 was positioned so that the top of its box was 101 cm radially from the centres of the 'RF limiters', comprising a pair of poloidal rings located 120° and 170° toroidally from the location of the poloidal array in the direction parallel to the plasma current. At this radial position the top of the box was 2 cm into the shadow of these limiters, which had a minor radius of 99 cm from a centre at R = 261 cm. This shadowing was necessary in order to limit the heat flux to the triton/proton probe box, but this position still allowed all relevant triton orbits to reach the detector aperture unobstructed by the RF limiters.

The scintillator itself was oriented so as to have a pitch angle detection range of $\chi \approx 40$–$90°$ with respect to the 'co'-direction of the toroidal field. Note that in this paper the pitch angle of the particle orbit χ is the angle of the particle velocity v with respect to the local *toroidal* magnetic field at the detector, i.e. $\cos \chi = v_{tor}/v$ (this angle is conveniently defined with respect to the fixed detector independently of the particular plasma current). This range was centred near the expected $\approx 60°$ pitch angles of the first-orbit losses by rotating the detector shaft about its axis 22.5° from the aperture-outward position into the 'co'-direction, so that the centre of the scintillator corresponded to a pitch angle of 67.5° in the co-direction with respect to the toroidal field. Note that particles approaching the detector with pitch angles of ≈ 85–$90°$ were blocked by the detector itself on the last orbit before entering the aperture. The aperture was 1.5 cm below the box top, see Ref. [24].

2.3. Geometrical resolution

The geometrical pitch angle and energy resolving capability of this detector illustrated in Fig. 3. Tritons and protons approach the front 'pinhole' aperture on helical orbits with gyroradii of approximately 5 cm and typical pitch angles in the range $\chi \approx 40$–$85°$. Particles which pass through both the pinhole and the 'slit' aperture are dispersed according to their pitch angle across one direction of the scintillator screen, as indicated. The same aperture pair also acts like a magnetic spectrometer and disperses particles according to their gyroradius along the orthogonal scintillator direction, also shown in Fig. 3.

A detector simulation code was written to clarify the geometrical resolution of this aperture/scintillator configuration. A set of helical orbits with a specified

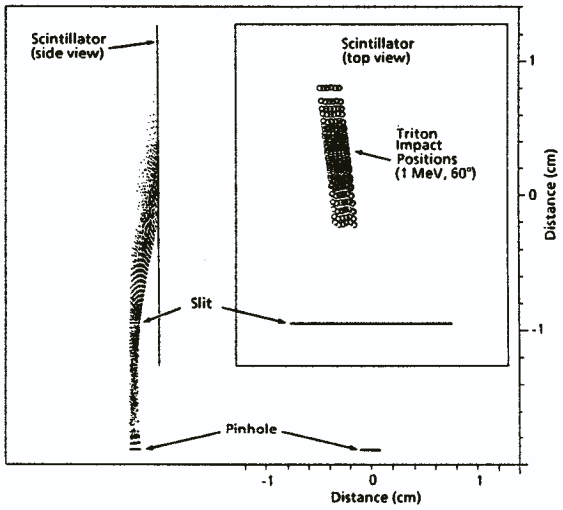

FIG. 4. Detector simulation code results for 1 MeV tritons incident at 60° pitch angle on detector No. 6. Each circle represents the scintillator impact position of one possible trajectory through the finite sized aperture pair. The pitch angle resolution is mainly set by the front aperture width and the gyroradius (energy) resolution is mainly set by the aperture heights.

incident pitch angle and gyroradius were constrained to pass through both the finite sized rectangular front and rear apertures, and the resulting particle impact positions on the scintillator were determined for various possible orbits allowed through the aperture pair. The actual angle of the normal direction of the aperture with respect to the toroidal field (22.5°) and the energy attenuation effect of the foil (see below) were also included in the code.

Typical results for detector No. 6 are shown in Fig. 4 for 1 MeV tritons with an incident pitch angle of $\chi = 60°$. For this case, the 0.2 cm wide front aperture sets a geometrical pitch angle resolution of about $\pm 3°$ at the scintillator, and the 0.1 cm high front and rear apertures set an energy resolution of about a factor of two, i.e. the FWHM points of the 1 MeV triton impact distribution coincide with the mean impact positions of 0.5 MeV and 2 MeV tritons. These results are consistent with analytical estimates of resolution used earlier [25].

Therefore, this detector design had relatively good pitch angle resolution, but poor energy resolution. The geometrical pitch angle resolution, in fact, was chosen to be about the same as the optical resolution. The relatively poor energy resolution was acceptable since the dominant energy spread was expected to be due to the relatively uninteresting beam-target Doppler shifts.

The aperture height also was limited by the need to eliminate the direct line-of-sight path through the aperture pair to the scintillator to prevent possible soft X-ray backgrounds.

2.4. Foil

Behind the slit aperture was a thin foil which blocked the plasma light and the low energy plasma particles from entering the scintillator region. The foil was 3 μm thick aluminium, which let pass both 1 MeV tritons (with about 30% energy loss) and 3 MeV protons (with $<3\%$ energy loss), but which stopped the 0.8 MeV ^{3}He ions created in D–D reactions. This foil also set a low energy cut-off for triton or proton detection of about 300 keV.

The foil also acted as a scatterer of tritons or protons passing through them. The scattering angle for tritons in the 3 μm aluminium foil is about 20 milliradian [26], which makes a slight contribution to the gyro-radius resolution (see Section 3.2), but has negligible effect on the pitch angle resolution.

To check for possible differences between triton and proton loss, detector No. 9 had an 18 μm aluminium foil which stopped the 1 MeV tritons but let pass (with $<20\%$ energy loss) the 3 MeV protons. The results from this proton-only detector were at least qualitatively similar to the results from the triton/proton detectors No. 6 and No. 11. Detector No. 4 for 15 MeV protons had a 275 μm stainless steel 'foil' and a very wide (non-energy resolving) aperture.

2.5. Scintillator

The scintillator, which was similar to that used in the prototype, consisted of a standard P11 ZnS(Ag) phosphor coating of 10–15 μm thickness (or 1–2 crystals) on top of a 2.5 cm $\times$ 2.5 cm $\times$ 1 mm quartz plate. A discussion of triton/proton detection with this scintillator can be found in Ref. [24].

A property of this P11 scintillator is that at temperatures above about 150°C it emits less light per particle than at lower temperature ('quenching'). The temperatures inside the probe box were monitored with thermocouples and never exceeded 100°C for all data in this paper.

It is plausible (but not experimentally demonstrated) that the light output of this scintillator is proportional to the energy deposited in it by various MeV ions. Previous estimates based on this assumption [24] concluded that in this scintillator a 1 MeV triton creates about 1/3 of the light of a 3.5 MeV alpha particle, and a 3 MeV proton creates about 1/3 of the light of a 1 MeV triton (since the proton range in ZnS is about 100 μm). Thus, about 75% of the light in this scintillator is expected to come from 1 MeV tritons and 25% from 3 MeV protons, assuming equal numbers of tritons and protons incident on the detector. On the basis of this assumption, the absolute calibration for tritons and protons was previously estimated from cross-calculations with bench-top alpha particle source (^{241}Am and ^{244}Cm).

2.6. Optics

Using a single f/2 quartz lens the scintillator image was transferred 35 cm down a shaft, across a vacuum window, and into the coherent fibre optic bundle. The optical characteristics of this system up to and including the video camera were calibrated before installation using a diffuse white light screen and a test pattern grid at the scintillator plane.

Through the 'blurring' of a sharp black edge on a white background the spatial resolution was found to be equivalent to about ± 0.2 cm at the scintillator plane, corresponding to a pitch angle resolution of about $\pm 5°$ FWHM. The relative sensitivity across the scintillator plane gradually decreased about 20% from centre to edge, mainly owing to 'vignetting' in the single-lens optical system. Also present was some 'blooming' in the video camera, particularly at high signal levels, which spread light from any bright object over adjacent parts of the image. It was difficult to precisely correct for this blooming effect, but most of its effect was automatically included in the estimate of spatial resolution.

The 8 m long coherent plastic fibre bundles had a 50 $\times$ 50 square array of 250 μm fibres (Mitsubishi Super-Eska, numerical apertures 0.46). These fibres were aligned to about ± 1 fibre, and were uniformly transmitting to within about $\pm 10\%$ across the array. The four plastic fibre bundles of the poloidal detectors were viewed together in a square array through an f/2 lens by the video camera.

2.7. Signal detection

The calculated detection efficiency (detected triton flux divided by global triton production) was typically $\epsilon \approx 10^{-8}$ and so, at a global triton source rate of $\approx 10^{16}$ tritons per second, the expected flux onto the scintillator was $\approx 10^8$ tritons per second. This rate was far too high for pulse counting and therefore only light flux measurements were made.

The light flux from the plastic fibre bundle was detected in one of two ways: either a gated, intensified video camera was used to digitize the 2-D images versus time, with 32 ms between video fields, or a linear array of eight 0.1 cm dia. plastic fibres was used to transfer the light from selected parts of the bundle to eight discrete photomultiplier tubes.

The video camera mode was used to evaluate the overall 2-D pattern of light at the scintillator and its slow time variation. The camera (Xybion model ISG-03) had a controllable microchannel plate gating time used to compensate for varying triton/proton source levels; typically, the gating time varied from 2 ms at high triton/proton levels to 16 ms at low levels. The camera also had an internal automatic gain control of the internal microchannel plate voltage, which was monitored by adding into its field of view a set of small but constant reference lights. The camera output was checked to be linear with respect to light input, but had a 15% negative offset (which was corrected for in the analysed data).

The photomultiplier (PM) tubes (Hamamatsu R762) were designed to look for fast fluctuations in the lost triton/proton flux. The fibres leading to the PM tubes (0.1 cm dia. Mitsubishi Eska-Extra) were proximity coupled to (i.e. directly touching) the 50 × 50 2-D bundle so as to cover eight different pitch angles near the peak in the gyroradius co-ordinate (this obstructed the view of the bundle from the camera). The current from the PM tubes was monitored by the voltage drop across 100 kOhm resistors by an amplifier with a bandwidth of 20 kHz. The voltage signals were digitized at rates of (5–100) × 10^3 samples per second by standard TFTR electronics.

2.8. Data systems

The video camera data were transferred via a fibre optic link to the TFTR control room, where they were digitized with a PC-based video frame grabber board with 4 MB memory (42 fields) and simultaneously archived in standard analog video tape format. Customized image processing was available on the PC between shots. The video data were also sent to a VAX in compressed form (3 video lines × 3 pixels = one compressed pixel) for further image processing.

The PM data were archived on the standard TFTR computer system. The timing of the PM data with respect to other fluctuation diagnostic data was accurate to within 10 μs when the fastest digitization rates were used.

2.9. Backgrounds

The main background in this system was a uniform illumination of the whole coherent bundle area with a light intensity proportional to the total neutron flux from TFTR, evidently due to light created within the plastic fibre bundle by neutrons and/or gammas from the tokamak. This was checked by noting that the same background was seen on another plastic bundle of identical design which was run a similar distance inside the TFTR test cell ($\approx$3–4 m), but which was not connected to any triton probe or other source of light. Note that in 1987 this background was lower, since there was only $\approx$1 m bundle length within the TFTR test cell.

The relative neutron/gamma background was reduced by adding an optical filter matched to the blue emission spectrum of ZnS(Ag) between the ends of the plastic bundle in the basement and the signal detectors (Kodak Wratten filter No. 47). The remaining fibre bundle background was subtracted using an edge or a corner of the scintillator area not used for imaging the tritons.

The possible background caused by neutrons and/or gammas interacting with the scintillator itself [24] was apparently too small to be observed in this system. There was also no perceptible background due to hard X-rays from runaway electrons, except after a major disruption when the scintillators were often brightly lit by a transient runaway electron induced X-ray burst.

Note that the soft X-ray background in the prototype was successfully eliminated in the present detector by adding 0.3 cm of stainless steel shielding above the scintillator (see Fig. 2). The calculated reduction in the soft X-ray background was more than a factor of 100 and, in fact, no perceptible soft X-ray background was observed with the present system.

3. RESULTS FROM TFTR

This section describes the experimental results obtained mainly from the triton/proton detector No. 6 located near the bottom of the TFTR vacuum vessel. Particular attention is given to surveying a wide variety of TFTR conditions and to comparing the video camera and the PM signal detection modes.

Wherever possible, the results are compared with predictions from the PPPL single-particle first-orbit loss code ORBIT [17, 25]. This code uses either modelled or experimentally derived triton/proton source and plasma current profiles (from the PPPL analysis code SNAP), but it ignores collisional effects, toroidal field

ripple and MHD instabilities (the effects of which are discussed briefly in Section 4.2).

For simplicity, the combined triton and proton flux measured by dectector No. 6 will be called the 'triton' flux, despite the fact that the signals measured by the this detector contain a (calculated) 25% contribution from 3 MeV protons [24]. The 3 MeV protons and the 1 MeV tritons have exactly the same gyroradii and therefore should have exactly the same first-orbit loss.

Sections 3.1–3.10 present a detailed comparison between the measurements and the first-orbit loss model for the bottom detector (No. 6) for discharges with no strong MHD activity, Section 3.11 briefly describes observations of MHD induced triton loss, and Section 3.12 summarizes observations from other detector locations.

3.1. Typical 2-D image

A qualitative view of the triton imaging results is given in Fig. 5, which shows raw data from a typical 2-D image of light from the fibre bundle as measured by the video camera. The dark square near the borders of the plot corresponds to the boundary of the fibre bundle, the sides of which are about 10% larger than the image of the scintillator itself.

These data are from a standard 1.2 MA, R = 245 cm, a = 80 cm discharge which had 14 MW of neutral beam injection (NBI) for 0.7 s, with an average neutron (and triton) rate of 6×10^{15} neutrons per second over the beam duration. For this figure the data are averaged over the whole discharge, which included about 20 video fields during NBI, each exposed for 4 ms. The shaped of this pattern did not change significantly with time during this discharge.

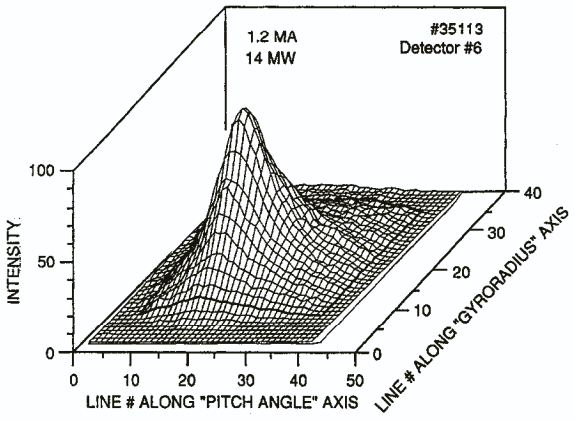

FIG. 5. Raw data of a typical 2-D pattern of light intensity from detector No. 6, showing the triton impact to be concentrated in one region of the scintillator plane. The boundary of the fibre bundle is shown by the darkened rectangle (the boundary of the scintillator is slightly smaller). These data were integrated over the whole NBI phase of a 1.2 MA discharge (No. 35113).

The scales in Fig. 5 refer to the number of lines or pixels along each axis after a 3 × 3 compression; the actual video image of this detector covered 3 × 41 = 123 horizontal lines and 3 × 40 = 120 vertical lines. Note that this image is not yet corrected for the 15% negative offset of the video camera. Also, for this case, the blue filter was not inserted (see Section 2.9), which caused the fibre bundle background to be somewhat larger than usually.

Note that the grid lines in this plot are oriented along the square scintillator boundaries, uncorrected for the polar geometry of the pitch angle versus gyroradius co-ordinates implicit in the detector design (see Fig. 3). The horizontal axis in Fig. 5 corresponds (approximately) to the pitch angle co-ordinate of the scintillator and the vertical (into the page) axis corresponds (approximately) to the gyroradius co-ordinate of the scintillator (this co-ordinate is roughly proportional to the square root of the particle gyroradius [25]). These geometrical distortions are accounted for in the following discussions of the gyroradius and pitch angle distributions.

The qualitative result from this figure is clear and is representative of all the data collected, namely, there is a single, fairly well localized peak in the 2-D image from the scintillator the position of which does not significantly change as the neutron rate varies with time during the discharge.

3.2. Typical flux versus gyroradius

The first-orbit loss model predicts that tritons will be lost with very nearly their birth energy, since the time for one orbit (< 10 μs) is much less than the collisional slowing down time ($\simeq 0.5$ s). The triton birth energy is 1.0 ± 0.2 MeV, the spread being due to the Doppler shift of beam–target reactions at a deuterium beam energy of ≈ 100 keV. Thus, the gyroradius of lost tritons should be constant to within about $\pm 10\%$.

Figure 6 represents a vertical 'slice' through the peak signal region of the 2-D image of Fig. 5 (lines #14–21), showing the light flux along the 'gyroradius' co-ordinate of the scintillator. The distance along the scintillator is measured both in centimetres from the

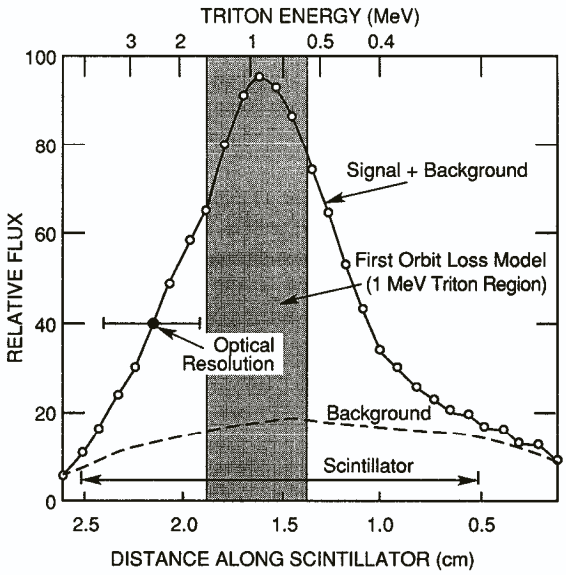

FIG. 6. Gyroradius distribution of the light intensity across the peak of the signal in Fig. 5. The peak signal came at an inferred triton energy of 1 MeV, with FWHM ranging from 0.5 to 2 MeV. This broadening is expected because of the finite aperture size and the optical resolution.

midpoint between the front and rear apertures (bottom scale) and in terms of the inferred triton energy (top scale). The inferred triton energy is calculated by the detector simulation code for an incident triton at a 60° pitch angle (see Section 2.3), including the foil energy attenuation effect.

The background curve in this figure is the intensity versus the line number for the same discharge, evaluated at a position at the edge of the sinctillator where the triton flux is expected to be negligible (lines #30–34). Since the background from the plastic bundle itself is fairly uniform across the scintillator area, as was seen in cases with the bundle disconnected from a probe, this curve should approximately represent the background under the peak signal curve. Note that neither the signal nor the background curves are corrected for slight vignetting and blooming in the camera (see Section 2.6).

The peak of the net signal is very near the position expected for 1 MeV tritons. This is observed on all discharges at this toroidal field of ≈48 kG. The location of this peak was shifted substantially with a lowered toroidal field, just as expected from the gyroradius change for 1 MeV tritons [25]. Note also that the peak of the expected 3 MeV proton signal should be shifted only a small distance (<0.1 cm) from the triton peak because of the relatively lower foil attenuation effect.

The width of the observed signal appears to cover an inferred energy range of ≈0.5–2.0 MeV. However, several sources of broadening are expected for 1 MeV triton first-orbit loss in this detector: (1) the Doppler spread in triton energy of ±20% or, equivalently, about ±0.2 cm along the scintillator; (2) the expected geometrical spread due to the 0.1 cm front and rear aperture heights in this detector, which, as indicated by the shaded region in Fig. 6, corresponds to a root mean square (rms) spread of about ±0.25 cm (see Section 2.3); and (3) the expected spread in this direction due to multiple scattering in the foil, which is about 0.1 cm for 1 MeV tritons (see Section 2.4).

Combined with these sources of broadening is the 'optical resolution' of about ±0.2 cm (see Section 2.6), indicated by the horizontal error bar on the data in Fig. 6. Together, these four factors create an expected width of about ± 0.4 cm, which is quite close to the observed ±0.4 cm FWHM signal width. There is also a systematic uncertainty of about ±0.1 cm in the alignment between the experimental curves and the horizontal position scales (not shown).

The conclusion which can be drawn from this result is that the observed position of the peak of the signal along this gyroradius co-ordinate is consistent with the detection of the first-orbit loss 1 MeV tritons (and 3 MeV protons). Note, however, that the precise shape of the gyroradius distribution cannot be determined at the present system resolution; thus the potential presence of a small population of lower energy particles, for example due to collisional loss effects, cannot be excluded by this measurement.

3.3. Typical flux versus pitch angle

The expected pitch angle dependence of first-orbit loss is sharply peaked around a 'critical angle', which corresponds to the pitch angle of the fattest banana orbit for 1 MeV tritons going through the given detector position [25]. A typical example of this variation of the orbit trajectory with pitch angle is shown in Fig. 7(a). At the critical pitch angle of ≈55°, the trajectory or 'sightline' of the orbit passes nearest to the high triton source rate region near the plasma centre, and so the escaping flux should be largest at this pitch angle. Figure 7 is drawn for a plasma current of 1.6 MA, but a similar drawing can be made for the normal current range of TFTR (0.8–2.0 MA).

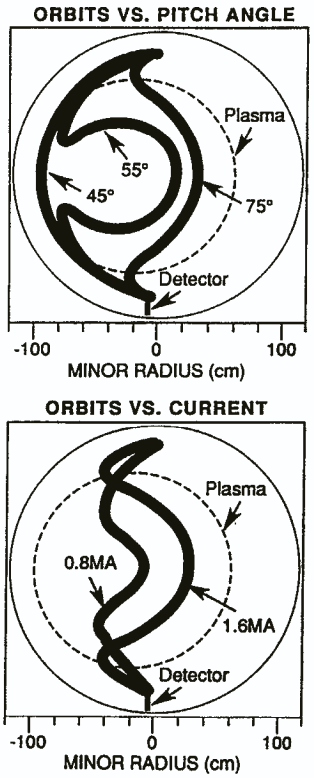

FIG. 7. Calculated trajectories of some typical 1 MeV triton orbits which pass through detector No. 6.
(a) Orbits for three pitch angles, all for a plasma current of 1.6 MA and for a fixed plasma current profile. The fattest banana orbit occurs at a 'critical angle' of ≈55° when the orbit most closely approaches the plasma centre and the largest triton flux is expected.
(b) Orbits for 65° pitch angles for 1.6 MA and 0.8 MA, illustrating the expected decrease in flux with increased current.

Figure 8 represents a horizontal 'slice' through the peak signal region of the 2-D image presented in Fig. 5 (lines #15–22), showing the light flux versus the pitch angle co-ordinate at the scintillator. The distance across the scintillator is measured in centimetres from its geometrical centre, which is aligned to correspond to a pitch angle of 67.5° with respect to the 'co'-direction of the plasma current. The pitch angle scale at the top is calculated from the detector simulation code for this horizontal slice position, i.e. including the slightly polar geometry and the effect of the foil on the particle gyroradius. The approximate background curve is estimated from a set of lines at the edge of the scintillator where no tritons are expected (lines #28–32). Again, these curves are not explicitly corrected for the slight vignetting and blooming effects in the camera.

The peak of the observed signal in Fig. 8 is at a pitch angle of about 55° with respect to the toroidal 'co'-direction. This is quite near to the expected critical pitch angle of 59° calculated by the first-orbit loss code at 1.2 MA for 1 MeV tritons at this detector, as shown by the solid region in this figure. The calculated critical pitch angle is constant to within about ±2° for reasonable variations in the assumed plasma current profile, here taken to be parabolic-cubed, with a Shafranov shift of 0.2a (for comparison, with zero Shafranov shift, the critical pitch angle shifts from 59° to 57°). There is also a systematic uncertainty in the optical alignment of about ±0.1 cm, or ±3° (near 60°), not shown in the figure.

Note that this idealized first-orbit loss curve in Fig. 8 does *not* include the expected ±3° geometrical pitch angle broadening due to the 0.2 cm width of the front aperture (see Section 2.3), or the broadening due to the ±20% Doppler energy spread in triton energy, or the effect of averaging over the lines used to obtain the experimental curve — the latter two of which produce each a spread of about ±1° in the predicted peak. Thus, the expected broadening of the model curve is about ±4° around the idealized shape.

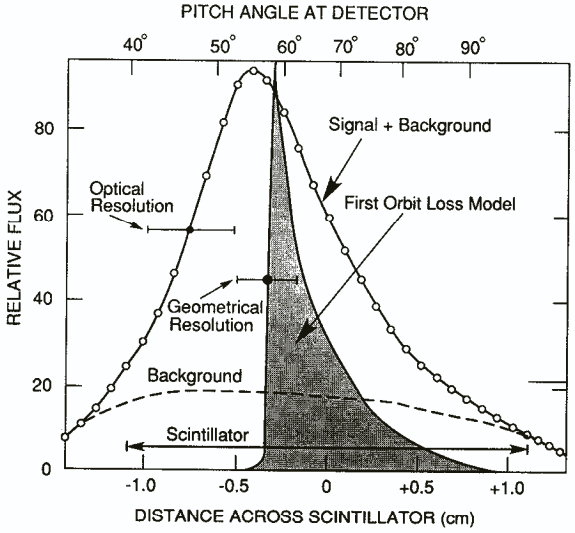

FIG. 8. Pitch angle distribution of the light intensity across the peak in the signal of Fig. 5. The maximum signal came at an inferred pitch angle of ≈55°, which is close to the peak in the calculated curve at 59° indicated by the shaded region. The broadening of the signal curve with respect to the simplified model curve is expected from the detector's geometrical resolution (error bar on the shaded curve) and the optical resolution (error bar on the data). There is also an uncertainty of ±3° in the pitch angle alignment of the detector (not shown).

Thus, the combined widths of the idealized model curve (about ±5°), the expected instrumental broadening (±4°) and the 'optical resolution' (±5°) lead to an expected signal width of about ±8°, which at present we interpret to be in reasonable agreement with the observed width of ±10°. Unfortunately, the precise shape of the pitch angle distribution and the expected sharp drop in flux below the critical angle cannot be identified with the present system resolution.

The conclusion which can be drawn from this section is that the position and width of the light signal versus the pitch angle is consistent with the expected first-orbit loss. Small variations in the peak of the pitch angle distribution with varying plasma current are discussed in Section 3.7.

3.4. Typical flux versus time

Figure 9 shows the light flux versus time for the discharge discussed in Sections 3.1–3.3, as monitored by the video camera and averaged over the centre of the peak region (horizontal lines #14–21, vertical lines #15–22). The time dependence of the peak light flux approximately follows the neutron signal monitored by the standard epithermal neutron detectors [27]. The background, which was evaluated at the corner of the scintillator, also follows the neutron flux as expected.

This rough linearity between the lost triton flux and the neutron flux is typical of all discharges without strong MHD activity. This behaviour is also qualitatively consistent with the expected prompt first-orbit loss, since the loss time is only ≈10 μs. However, the triton source and current profiles can also affect the ratio of lost tritons to neutrons in a given discharge at a fixed plasma current (see Section 3.9). These and other time dependent effects are more conveniently monitored using the photomultiplier detection mode, as described next.

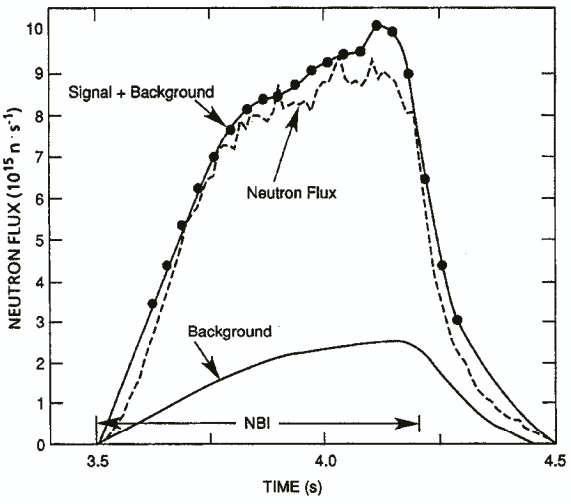

FIG. 9. Time dependence of the peak signal from the discharge used for Fig. 5, as digitized from the video camera data with a time resolution of 32 ms. The net triton signal follows the time dependence of the 2.5 MeV neutron flux, as expected for first-orbit loss. The background signal due to neutron/gamma induced light in the fibre bundle was monitored using a corner of the scintillator not used for triton detection.

3.5. Typical photomultiplier signals

For most of the 1988 runs, the triton light signals from detector No. 6 were monitored with the eight-channel PM array instead of with the video camera (Sections 3.1–3.4). This was done by proximity coupling eight plastic fibres directly to the coherent fibre bundle. These eight fibres were distributed along the approximate pitch angle direction of the scintillator near the peak of the signal in the gyroradius directions, using either 0.1 cm or 0.2 cm spacing between fibres. Note that for all PM data discussed here, the blue filter was used to reduce the background light level from the plastic fibre bundle (see Section 2.9).

Typical pitch angle distributions inferred from these fibres are shown in Fig. 10 for three discharges, including a 1.2 MA (15 MW) discharge similar to that discussed in Sections 3.1–3.4 (using the video camera), and discharges at 2.0 MA (17.5 MW) and at 1.0 MA (17.5 MW). For this figure the signals were integrated over 0.5 s during NBI when there was no strong MHD activity, and normalized by the averaged neutron flux over this period.

These pitch angle distributions all have a peak near 58° similar to the distribution obtained with the video camera monitor (Fig. 7). The widths of these distributions appear to be about ±(5–10°), i.e. somewhat narrower than the ±10° inferred from the video camera. This was expected because of the absence of the camera lens and some slight camera 'blooming' in the video mode. However, in this PM mode the discrete fibre spacing of about 5° limited the pitch angle resolution. In the PM mode there was also an extra background from neutron/gamma pickup in the PM tube fibres or in the PM tubes themselves; this was checked by decoupling these fibres from the coherent bundle and still observing half the background used in Fig. 10.

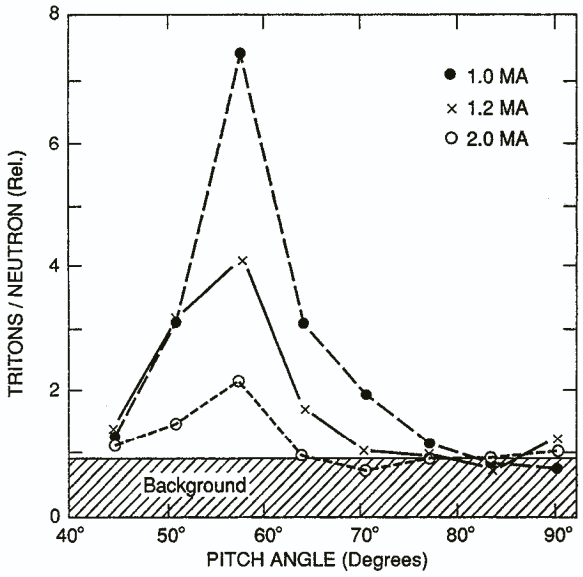

FIG. 10. Pitch angle dependence of the light flux as determined by the monitoring system of the photomultiplier tube (PM). The results for a 1.2 MA discharge (37054) are similar to the video camera results of Fig. 8. Other discharges at 1.0 MA (37063) and 2.0 MA (37068) have similar pitch angle dependences.

The time dependences of two of these PM channels for the 1.2 MA discharge are shown in Fig. 11, smoothed with a 10 ms averaging interval. Both the peak signal channel at about 58° and the background channel at about 83° have a time dependence similar to that of the neutron signal, as expected from the video camera result in Section 3.4.

The conclusion which can be drawn from this section is that the results from PM tubes are consistent with those from the video camera with respect to the pitch angle and time dependences of the signals, as illustrated by a typical 1.2 MA discharge.

3.6. Flux versus plasma current

As discussed in Section 1.1, the first-orbit confinement of MeV ions should be determined mainly by the plasma current and should improve dramatically over the range $\approx$0.5–2.0 MA. An illustration of this effect is given in Fig. 7(b), where at 0.8 MA the trajectories of 1 MeV tritons from the plasma centre can reach the bottom detector, whereas, at 1.6 MA, only the trajectories from about r/a > 0.3 can do so.

The typical variation with plasma current of the overall 2-D pattern of triton flux at the scintillator is shown in Fig. 12. This set of data comes from a plasma current scan for 0.9–1.4 MA and includes the 1.2 MA discharge used in Sections 3.1–3.4. The NBI power for this data set was 12–14 MW, the plasma radii were R = 245 cm and a = 80 cm, and the toroidal field was B = 46 kG.

Each photo of Fig. 12 shows raw data from a single video field exposed for 4 ms and chosen at a time during NBI when the instantaneous neutron flux was $(4.5 \pm 0.5) \times 10^{15}$ neutrons per second. For the light intensity displayed here, a linear false-colour scale was used, where yellow-white represents the brightest region and blue the dimmest region. Note that the scintillator area itself is indicated by the black corners in the 1.2 MA case and that the data retain the small negative offset of the video camera.

The qualitative result is clear and is typical of all results under MHD quiescent conditions. Namely, the shape of the gyroradius and the pitch angle distributions of the light flux are approximately independent of plasma current, and the total light flux decreases substantially with increasing plasma current at a fixed neutron source rate. The independence of the gyroradius distribution on plasma current implies that the escaping triton energy distribution is peaked at about 1 MeV, independent of current, as expected for first-orbit loss. The approximate independence of the pitch angle distribution on plasma current follows from the approximate invariance of the critical pitch angle on plasma current (see Section 3.7).

A quantitative analysis of the total escaping triton flux on the plasma current for the current scan over 0.9–1.4 MA (Fig. 12) is shown in Fig. 13. Here the

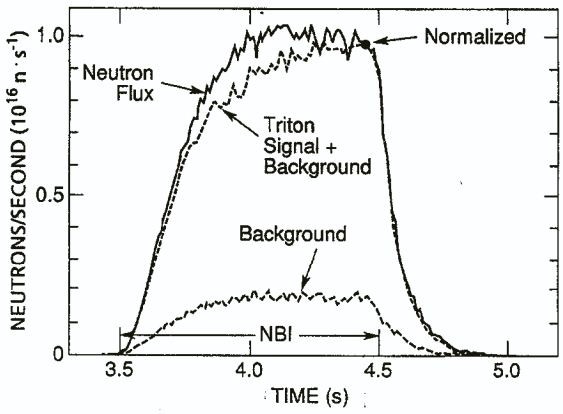

FIG. 11. Time dependence of the light flux from a single PM fibre positioned near the peak of the 2-D light distribution (58° pitch angle) for the 1.2 MA discharge of Fig. 10. The result is similar to that for the video camera monitor in Fig. 9.

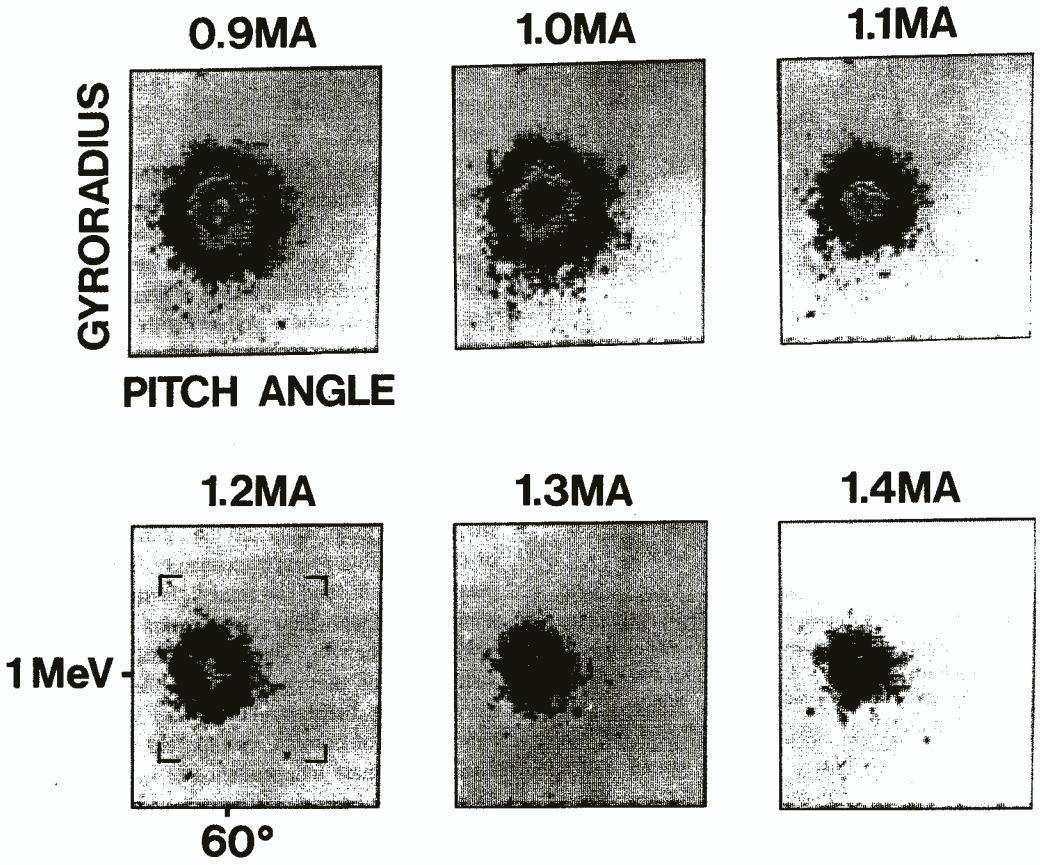

FIG. 12. Overall pattern of the escaping triton flux versus plasma current. Each of these pictures shows raw data from a single video frame exposed for 4 ms when the neutron flux was (4.5 ± 0.5) × 10^{15} $n \cdot s^{-1}$. The position of peak intensity was roughly invariant at ≈60° pitch angle and 1 MeV inferred triton energy, while the intensity decreased with increasing plasma current, as expected for first-orbit loss. The boundary of the scintillator itself is indicated by the four corners in the 1.2 MA case.

light flux for each of 15 shots was measured from single video frames, again exposed for 4 ms when the neutron flux was (4.5 ± 0.5) × 10^{15} neutrons per second. Points representing both the peak signal region (defined as in Section 3.4) and the average signals (over the scintillator area) are shown, with the background subtracted using a region inside the scintillator area but outside the peak region. Both measures of escaping triton flux per neutron, i.e. the relative triton loss fraction, decrease by about a factor of three between 0.9 MA and 1.4 MA.

A second test of the current dependence was made in the PM mode, with results as shown in Fig. 14. This data set came from a different current scan monitored over a somewhat larger current range (0.8–1.6 MA), with an NBI power of 7–28 MW, plasma radii R = 245 cm and a = 80 cm, and a toroidal field B = 48 kG. This figure includes 73 high

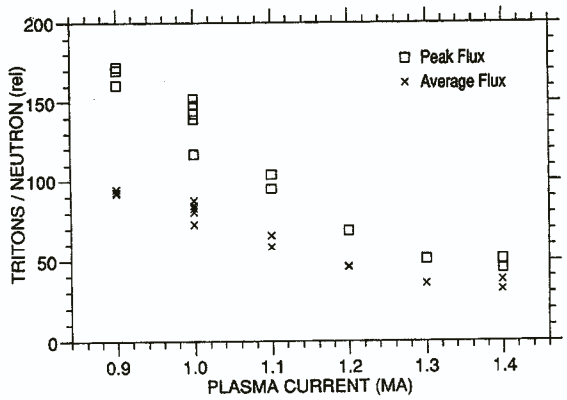

FIG. 13. Triton loss fraction versus plasma current for the data set used partly for Fig. 12 (35106-35123). The peak triton flux drops by about a factor of three over this current range.

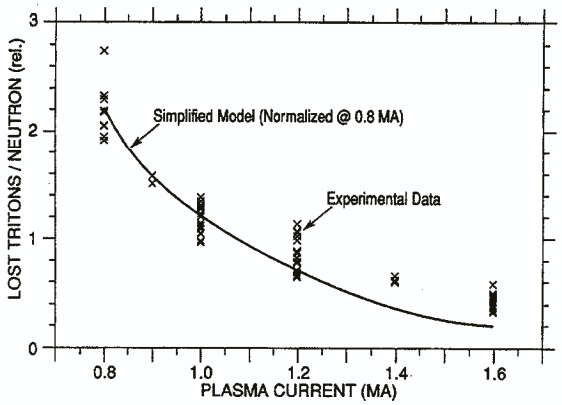

FIG. 14. Triton loss fraction versus plasma current for a series of discharges monitored with the PM detectors (35205–35453). The measured flux decreases approximately as expected from a simplified first-orbit loss model in which the profiles are kept constant. The background level, as monitored by another fibre, is constant as 0.1–0.2 on this scale, and has already been subtracted.

power, neutral beam heated discharges, where each point represents the net triton flux seen by the fibres for one discharge (i.e. the sum of the three PM signals that were within the peak in the pitch angle distribution, minus the background level measured at the edge of the scintillator), normalized by the total neutron flux during the same integration time. The integration times during NBI varied from 0.08 s to 1.5 s for these shots.

The resulting normalized triton flux, or relative triton loss fraction, decreases by about a factor of six between 0.8 MA and 1.6 MA, and by about a factor of three between 0.9 MA and 1.4 MA, similar to Fig. 12. Note that the background as monitored at the edge of the scintillator was small and constant for this data set, i.e. between 0.1 and 0.2 on this scale for all currents. A similar plasma current dependence can also be seen in the pitch angle resolved PM data for three different currents in Fig. 10. The results obtained using a single fibre near the peak are similar to those obtained with the summed triton signals in Fig. 14, since the pitch angle distribution did not vary substantially over this current range.

This observed decrease of the relative triton loss fraction with plasma current roughly agrees with the prediction of the simplified first-orbit loss model, as indicated by the theoretical curve normalized to the data of Fig. 14 at 0.8 MA. This model curve represents the total expected 1 MeV triton loss integrated over the pitch angle range ≈ 50–$80°$ for this detector, calculated assuming a constant triton source profile (parabolic to the sixth), a constant plasma current profile (parabolic to the third) and no Shafranov shift in the current distribution.

However, the simplified model used in Fig. 14 is not entirely consistent with the data, since this model predicts a factor of 11 reduction in triton flux per neutron over the same current range, and not the observed factor of six reduction. Part of this discrepancy may simply be a systematic underestimate of the background (and so an overestimate of the signals at high current), which could be due to a lower optical efficiency for the fibre at the edge of the scintillator compared to the fibre near the centre. Another apparent inconsistency with the first-orbit loss model is the apparent scatter of about $\pm 25\%$ rms in the data at fixed plasma current. Attempts to explain these effects in terms of systematic variations in the plasma current and/or the triton source profiles are discussed in Section 3.9.

The conclusion from this section is that the lost triton flux decreases with increasing plasma current at least qualitatively, as expected from the first-orbit loss model. If the poloidal distribution of this loss were invariant with current, the observed decrease would imply that the triton loss fraction at 1.6 MA must be $< 16\%$, since the loss at 0.8 MA can be at most 100%, which would imply good 'single-particle' alpha confinement for reactor grade machines. However, the actual poloidal distribution of triton loss (particularly near the outer midplane) remains to be determined.

3.7. Effect of plasma current on pitch angle distribution

Figure 15 shows video camera data for the pitch angle distributions of two of the discharges shown in

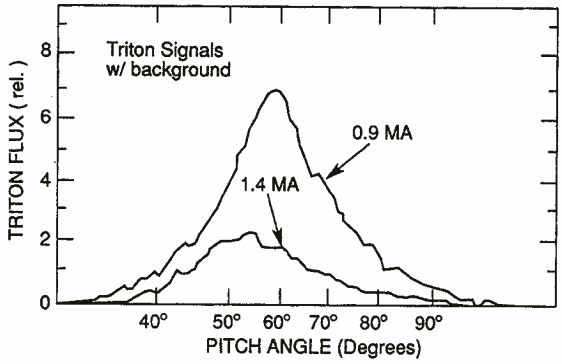

FIG. 15. Examples of pitch angle distributions for two of the discharges used in the current scan of Fig. 14. The signal peak is shifted to a lower pitch angle at the higher plasma current.

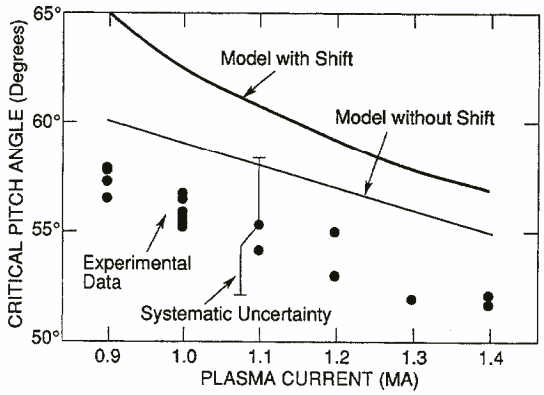

FIG. 16. Peak pitch angle of the measured triton flux versus plasma current for the data set of Fig. 14. The trend to lower pitch angles at higher current is predicted by the frist-orbit code. The model including the Shafranov shift in the profiles is probably the more realistic one.

the colour photos of Fig. 12. These raw data plots are averaged over the same gyroradius range as used in Fig. 8, but are displayed before 3 × 3 compression for better pitch angle resolution. In the higher current case, there is a shift of the peak towards lower pitch angles, which was seen consistently throughout the run.

Figure 16 shows this variation in the peak pitch angle for the set of shots used for Fig. 13. Experimentally, there is an ≈5° decrease in the pitch angle of the peak over the current range 0.9–1.4 MA, while the first-orbit loss models predicts a decrease of 4–7°. The model curves are shown for a simplified parabolic-cubed, unshifted current profile and also for the actual Shafranov shifted current profile (as inferred from neoclassical resistivity for individual TFTR shots over this current range), indicating that this expected decrease in pitch angle is not sensitive to the assumed current profile.

Thus, the relative change of the pitch angle distribution with plasma current agrees fairly well with the first-orbit model, although the absolute pitch angles of the points are consistently about 5–7° lower in pitch angle than those obtained in the Shafranov shifted calculation. This discrepancy is apparently larger than the estimated ±3% uncertainty in the absolute calibration of pitch angle at the scintillator (see Section 2.3).

3.8. Variation of flux with neutron source strength

As is evident from the plot of the relative triton loss fraction (Fig. 14), the lost triton flux increases approximately linearly with the global neutron (triton) creation rate at a given plasma current. For that data set the observed ±25% rms scatter in the relative triton loss was not correlated with the neutron source strength or the integration time. The approximate linearity between neutron source strength and escaping triton flux is also implicit in their similar time dependences, as shown previously in Figs 9 and 11.

This dependence is made explicitly using a data set for 1.6 MA plasmas in Fig. 17. These data include 169 (randomly chosen) 1.6 MA, 10–30 MW, R = 245 ± 2 cm, B ≈ 49 ± 3 kG, NBI shots from a month-long TFTR run period where the setup of the PM fibres was held constant, including 114 discharges without perceptible MHD activity (x). This data set includes none of the discharges discussed so far.

The relative triton loss fraction was obtained using the time averaged signal from the fibre nearest the peak flux (≈58°), after subtracting the signal from a fibre near the edge of the scintillator (83°) and normalizing the result by the integrated neutron flux during the NBI period. The integration time during NBI varied from 1.6 s (covering the entire NBI phase) to 0.08 s. Note that the neutron normalized background level itself was approximately constant at 0.7 ± 0.1 in these units for all shots, i.e. about 30% of the net signal level.

The result from Fig. 17 is that the normalized triton flux is approximately constant over a factor of 15 in the neutron source strength (0.2–3.0) × 10^{16} n·s^{-1},

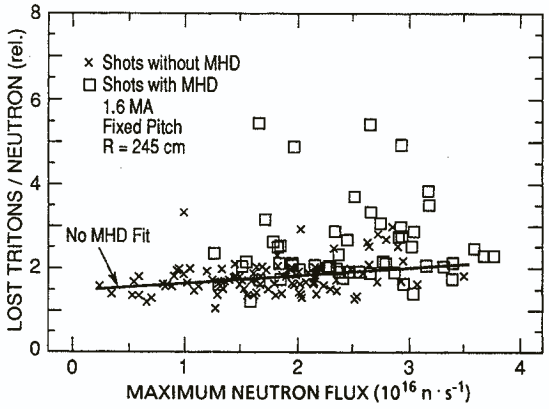

FIG. 17. Triton loss fraction versus neutron source strength for a large set of 1.6 MA discharges with nearly constant major radius R = 245 ± 2 cm (35365–37944). The average triton loss fraction does not vary significantly with neutron source strength for discharges without MHD activity, as expected for first-orbit loss with constant profiles. The discharges with MHD often have increased triton loss.

with the best linear fit to the data having only a 25% increase over this range. Thus, this result is at least qualitatively consistent with the first-orbit loss model, which predicts a constant triton loss fraction if the triton source and plasma current profiles are constant.

However, there is also an unexpected ±25% rms scatter around the mean for the discharges without MHD activity, with the highest and lowest points differing by a factor of two to three at a neutron rate of $\approx 3.0 \times 10^{16}$ n·s^{-1}. Note that most of this scatter is *not* due to shot-to-shot variations in the plasma or to statistical fluctuations, since the normalized triton loss for a consecutive sequence of discharges under constant plasma conditions typically varies by <10% rms.

There are several potential instrumental reasons for this scatter. One reason is day-to-day uncertainty in the relative calibration of the neutron detectors used for the normalization; however, with the best available neutron calibrations (as applied to Fig. 17), this uncertainty is about 5% [27]. Another reason is the day-to-day calibration of the PM tubes for the triton measurement, which was not monitored explicitly, but which is probably less than ±10% (since the voltage and configuration were not changed during the run and since there is no systematic trend in the scatter versus discharge number). A third possible reason is the typical ±10–20% variation in the triton-to-neutron ratio versus time during a discharge, as shown in Fig. 11; however, subsets of these data constrained to constant integration times had a similar scatter.

The conclusion which can be drawn from this section is that the approximate constancy of the normalized triton flux is consistent with the simple first-orbit loss picture, but there may also be some unexplained scatter in the data. Attempts to understand such variation in terms of triton source and plasma current profiles are described in the next section.

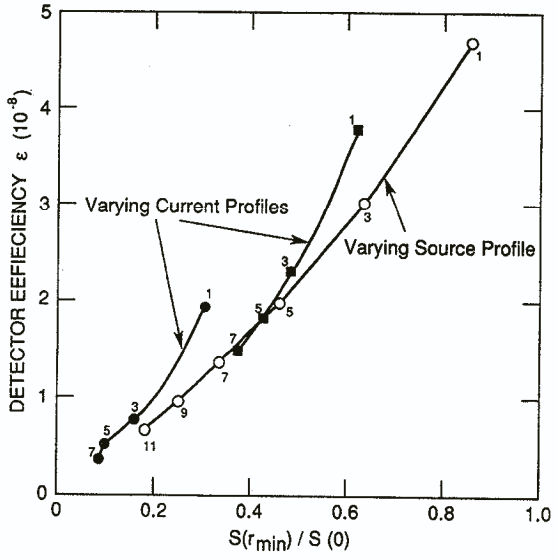

FIG. 18. Calculated effects of the triton source and plasma current profiles on the triton detection efficiency for detector No. 6 at 1.6 MA. The curves represent models with parabolic profiles to a power indicated by the number on the line. The experimental source profiles inferred from the SNAP code are typically fitted by a parabolic to the 7th to 9th power. Given these sensitivities, variations of a factor of two in detection efficiency over the discharges in the 1.6 MA database are to be expected.

3.9. Profile effects

The lost triton flux at a given plasma current can be affected by both the triton source profile and the plasma current profile. Generally, the lost triton flux is higher when the line integral of the triton source along its orbit is larger; this happens if the source strength becomes higher along the orbit, or if changes in the current profile shift the orbit to a region of higher source strength.

3.9.1. Calculated profile effects

The calculated effects of the source profile for 1.6 MA discharges are summarized by one curve in Fig. 18, where the calculated triton detection efficiency ϵ for the present detector is plotted versus the source profile shape factor $S(r_{min})/S(0)$; here, ϵ is the calculated triton flux through the aperture pair divided by the global neutron (triton) rate, $S(r_{min})$ is the local source rate at the distance of closest approach of the orbit to the plasma centre, r_{min}, which is independent of the assumed triton source profile, and S(0) is the triton source rate at the plasma centre. This figure is calculated for conditions similar to those for the data of Fig. 17, i.e. plasma radii of R = 245 cm and a = 80 cm, and a fixed current profile taken from one of the shots in Fig. 17 (No. 37084). The triton pitch angle at the detector was assumed to be 60°, for which case $r_{min}/a = 0.38$ (see Fig. 7). The triton source profile shape was varied from parabolic to the first power to parabolic to the 11th power, i.e. $S(r) \propto S(0)[1 - (r/a)^2]^p$, where the exponent p = 1–11 is indicated by the number along the curve. The implication of this result is that a variation of the triton source profile shape from $S(r_{min})/S(0) = 0.2$ to 0.4 can change the expected triton flux by about a factor of two.

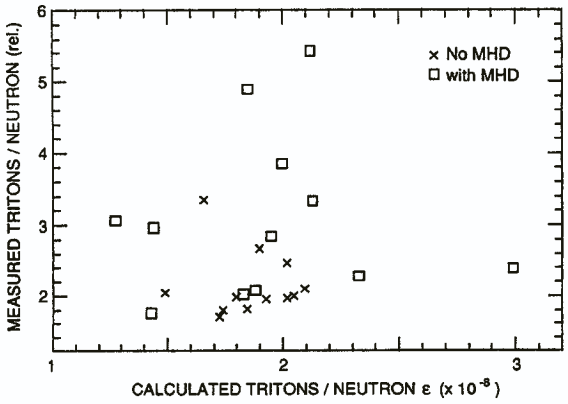

FIG. 19. Comparison between observed triton loss fractions and calculated detection efficiency using SNAP plasma current and source profiles for some shots in the 1.6 MA data set. The observed variations apparently cannot be identified with the calculated profile effects.

In Fig. 18 there are also two curves showing the calculated effect of the assumed shape of the plasma current profile on ϵ, taking into account the variation in r_{min} with current profile shape, given fixed source profiles. In both cases the current profile shape was assumed to be parabolic to a power varying from p = 1 to p = 7, with the power indicated by the number along the curves. The source profile shape was assumed to be parabolic to the fourth power for the curve on the right and parabolic to the tenth power for the curve on the left. The implication of these curves is that the current profile can also affect the expected value of ϵ by up to a factor of two, especially given the possibility of strongly driven or non-equilibrium current profiles in TFTR.

Thus, the observed variation of a factor of two to three between the lowest and the highest points in the experimental data of Fig. 17 is not inconsistent with possible profile effects. In Section 3.9.2, we attempt to find a correlation between experimental profile shapes and the scatter in the 1.6 MA data of Fig. 17.

3.9.2. Comparison with the data

One way to check for profile effects is to use the shot-specific triton source and plasma current profiles (including the Shafranov shift), as generated by the PPPL analysis code SNAP, in the triton detection effeciency code ORBIT, and to compare the computed efficiency with the observed effiency for each discharge. For a small but random set of 12 shots of the 114 shots without MHD used in Fig. 17, appropriate SNAP analyses were available for comparison, with results as shown in Fig. 19.

The computed efficiency varied over the range (1.5–2.1) × 10^{-8} for the shots with no MHD effects, apparently uncorrelated with the observed variation of a factor of two in the relative triton loss fraction, whereas a linear relation between the relative triton loss and the calculated efficiency would be expected from profile effects. A similar result applies to 12

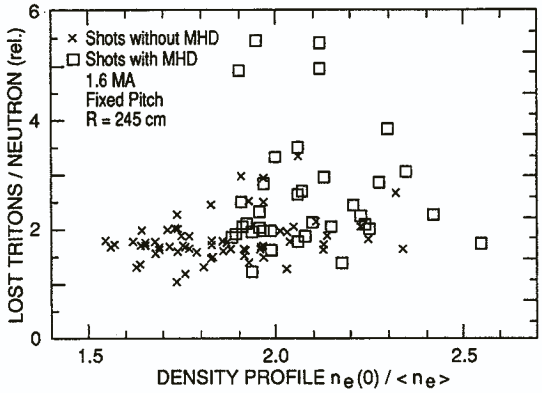

FIG. 20. Variation of the normalized triton flux with the electron density profile peaking factor. For discharges without MHD there is a slight trend towards increased triton loss at high values of this parameter, possibly associated with the broadened current profiles. The discharges are again from the 1.6 MA group at R = 245 ± 2 cm.

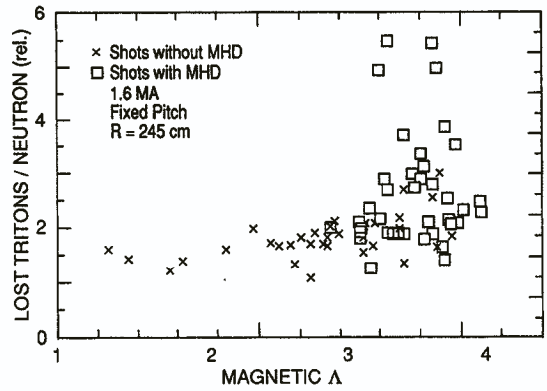

FIG. 21. Variation of the normalized triton flux with magnetically inferred Λ for the 1.6 MA data set at R = 245 ± 2 cm in Fig. 17. For discharges without MHD activity there is a slight tendency towards increased triton loss at high Λ, possibly associated with increased Shafranov shift.

other shots with MHD effects (see Section 3.11). Note that the analysed discharges without MHD fall in the range $S(r_{min})/S(0) \approx 0.3$, i.e. the typical experimental source profile was approximately parabolic to the seventh to ninth power (including beam–target and beam–beam sources).

Another way to look for possible profile effects is to plot the experimental triton efficiencies of Fig. 17 against some more directly measured experimental parameters related to profiles. This is done in Figs 20 and 21.

In Fig. 20 the triton data are plotted against the electron density peaking factor $n_e(0)/\langle n_e \rangle$, as determined from the multichannel interferometer system [28] at the time of maximum stored energy for each discharge. The region below $n_e(0)/\langle n_e \rangle \approx 2$ is conventionally considered the 'L-mode' regime of degraded plasma confinement, and the region above ≈ 2 is considered the 'supershot' regime of improved plasma confinement. The supershot regime has more centrally peaked neutron source strengths but broader current profiles than the L-mode regime (according to SNAP) — trends which tend to cancel each other with respect to triton detection efficiency. In the data, there seems to be a systematic trend for the lost triton detection efficiency of discharges without MHD to increase with the density peakedness parameter, as if the current broadening dominated the source peaking effect. However, this is not a large effect.

In Fig. 21 the triton data of Fig. 17 are plotted against the parameter Λ ($= \ell_i/2 + [\beta_{pl} + \beta_{p\perp}]/2$) for each discharge, as derived from magnetic measurements at the peak of the stored energy. Λ is a (nearly linear) measure of the Shafranov shift of the plasma centre with respect to the outermost magnetic flux surface. Evidently, there is a weak increase in the normalized triton flux with increased Shafranov shift (for discharges without MHD). Orbit code calculations for 1.6 MA discharges of this type show a 30% increase in the expected detection efficiency with increased Shafranov shift over this range (up to 0.2a). Incidentally, it is not surprising that the triton efficiency increases with neutron rate, density profile peaking and Λ, since these three parameters are correlated with each other (and with neutral beam power) in this database.

A similar attempt to find a correlation between the normalized triton flux and the plasma density itself showed only a slight increase of flux with density, which might be associated with broader triton source profiles at higher density. No correlation was found between normalized triton flux and central electron temperature.

A more successful attempt to demonstrate the profile effects was made using the current scan data of Fig. 14, in which it was observed that the decrease in the triton flux was less than expected when a simplified fixed-profile efficiency calculation was used. When SNAP generated profiles from shots in this sequence were used instead, the calculated detection efficiency ratio between 1.0 MA and 1.6 MA discharges was $2 \pm 0.5:1$, whereas the calculated efficiency ratio for the fixed profiles used in Fig. 14 was 6:1. Therefore, the experimental ratio of $2.5 \pm 0.5:1$ between 1.0 MA and 1.7 MA discharges is better fitted by the SNAP generated profiles, which incorporate the significantly broader source and current profiles calculated for the higher current cases.

The tentative conclusion is that any profile effects on triton loss at a fixed plasma current are too subtle to observe directly in the database at 1.6 MA, although the rather gross profile effects associated with differing currents can apparently be observed. Further understanding of these triton profile effects will probably require direct measurements of the 2.5 MeV neutron source and plasma current profiles (which were not routinely available during the 1988 run).

3.9.3. Other possible profile effects

Finally, we mention two other possible profile effects. The first concerns the influence of the NBI direction and the second concerns the effect of time varying plasma current.

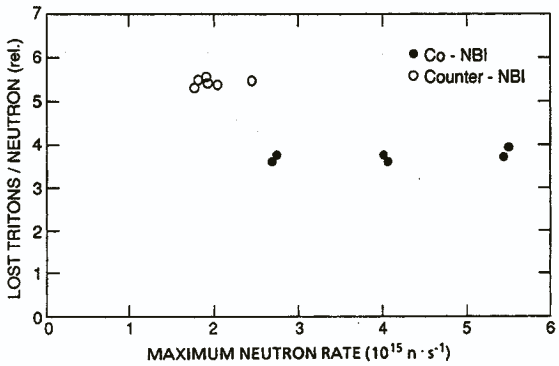

FIG. 22. Variation of the normalized triton flux with co- and counter-balance for a set of unidirectional NBI discharges at 1.1 MA. There is a significantly higher flux for counter-injection cases; however, this trend cannot be explained by calculated profile effects.

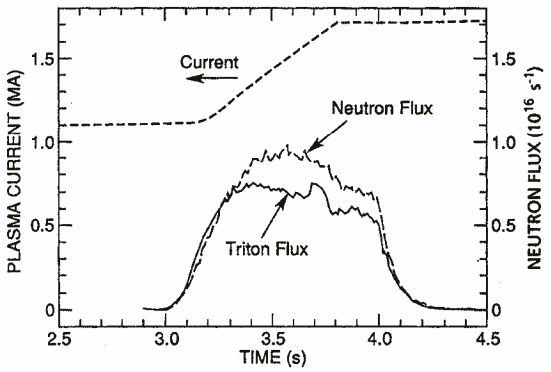

FIG. 23. Variation of the triton loss fraction with time during a current ramp discharge. The observed flux drops by only 30% between 1.1 MA and 1.7 MA, compared to the expected three times larger drop as observed for normal steady state discharges, suggesting a large profile broadening effect during this ramp.

The effect of NBI direction is shown in Fig. 22 for a set of 1.1 MA data, for either co-injection (i.e. along I) or counter-injection (note that the data in Fig. 17 are mainly for balanced injection). The consistent result of these and other cases was that the normalized triton flux was about 40% higher for counter-injection than for co-injection, with balanced injection being nearer to the levels for co-injection (a similar effect can also be seen in discharges with time dependent changes in NBI direction). However, neither the calculated triton source profiles (including beam–beam reactions) nor the calculated plasma current profiles (including beam driven currents), were significantly different for co-injection and counter-injection, as analysed by SNAP and TRANSP.

An alternative explanation for the effect of co- and counter-injection is that the triton birth distribution became significantly anisotropic in velocity space because of the Doppler shift of the beam–beam and beam–target reactions, causing the sightline integrated triton loss to be dependent on the sign of this anisotropy (the present orbit efficiency code assumes an isotropic source). The expected effect of this anisotropy would be in the observed direction, namely an increase in the lost flux when more reactions are produced in the counter-direction near the plasma centre.

A second effect is illustrated in Fig. 23, which shows the influence of a time dependent plasma current 'ramp' on the normalized triton flux. In this case, the normalized flux decreased by only about 30% when the total plasma current is raised from 1.1 MA to 1.7 MA, in contrast to the factor of three decrease expeced from the data of Fig. 14 and the factor of six decrease expected from calculations assuming fixed plasma current and source profiles. Apparently, the time dependent profiles are much broader in this ramp case, leading to a relatively high triton loss. A simulation of possible 'surface' current profiles was made with the ORBIT code; this showed that if the additional 600 kA of plasma current was localized near r/a = 0.8, then the expected triton flux decreases by only a factor of two. However, further interpretation of these discharges is complicated by MHD activity during the current ramp, which appears in this case at 3.7–3.8 s.

3.10. Effects of plasma position

The effects of plasma position on the escaping triton flux are shown in Fig. 24. For these discharges (all at 1.4 MA) the normalized triton flux (summed over pitch angle) is shown for positions of the plasma major radius of R = 238 cm, 245 cm (the standard position) and 252 cm. The striking observation is that the triton loss fraction at R = 238 cm is larger by a factor of about two to three than that at R = 245 cm or that at 252 cm. This trend has consistently been observed on several different occasions during the 1988 runs.

Application of the ORBIT code to these different plasma positions predicts that the triton flux should be approximately independent of plasma major radius, since for a given pitch angle the triton orbit tends to move along the plasma flux surfaces. In fact, the code predicts a 30% *decrease* in flux at R = 238 cm, compared with that at R = 245 cm, when using SNAP generated source and plasma current profiles for discharges in this data set.

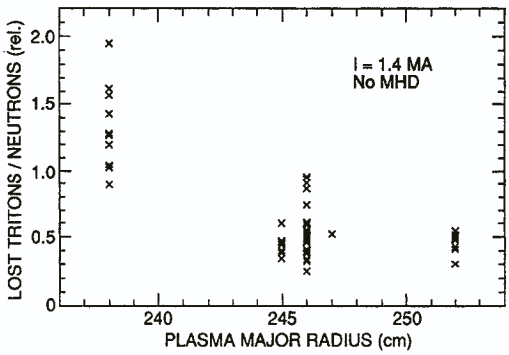

FIG. 24. Effect of plasma major radius on triton loss fraction for a set of 1.4 MA discharges (36365-37994). There is an unexpected increase in flux for the small major radius plasmas.

One possible explanation of this discrepancy is that the finite spacing between PM fibres (see Fig. 10) allowed small shifts in the pitch angle distribution to affect the total signal seen by the fibres (i.e. the peak signal at R = 245 cm may have occurred between two adjacent fibres, resulting in an underestimate of the net signal). However, the orbit code predicts that the peak of the pitch angle distribution should shift from 59° at R = 245 cm to 56° at R = 238 cm and to 60° at R = 252 cm, which seems too small a shift to cause the observed variation in net signal. In fact, examination of the pitch angle distributions versus R shows, if anything, a slight *increase* in the peak pitch angle at R = 238 cm, in contradiction to the orbit code.

Therefore, it seems that the R dependence of the lost triton flux shown in Fig. 24 cannot be understood at present on the basis of the first-orbit loss model. Possible explanations could involve unexpectedly broad profiles in these plasmas (compared with those calculated by SNAP) or MHD activity (however, low frequency MHD was not observed on these triton signals at R = 238 cm). Such effects are suggested by the fact that the triton loss fraction at R = 238 cm for these discharges was almost linearly correlated with the neutron rate, suggesting some systematic anomaly with increasing stored energy in these cases.

Note that the vertical position was not varied significantly during the 1988 run; however, earlier results showed no significant change in the escaping triton flux with vertical position changes of a few centimetres, in agreement with the orbit code.

3.11. MHD effects

Large coherent MHD activity was often observed to increase the triton loss, particularly in discharges at higher currents, as shown in the 1.6 MA database plot of Fig. 17 [16, 29]. At this current, about 30% of the high power discharges (>10 MW) had perceptible coherent oscillations on the triton PM signals near the region of peak pitch angle, $\chi \approx 50$–$70°$ (with no oscillations on the background channels at other pitch angles). Sometimes these oscillations persisted through most of the NBI phase and resulted in increased average loss, while at other times the MHD activity was either too weak or too brief to affect the integrated loss. The triton loss fraction for discharges without MHD in the 1.6 MA database was 1.8 ± 0.4 (in the units of Fig. 17), while for shots with MHD it was 2.5 ± 1, indicating a marginally significant increase overall with MHD.

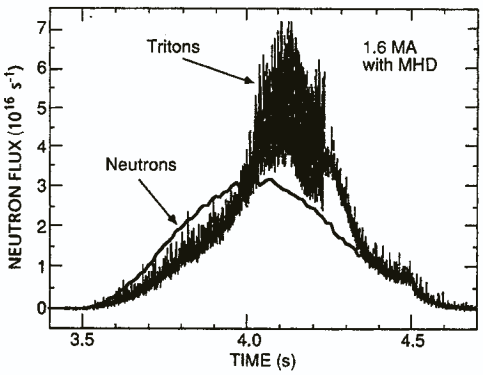

FIG. 25. Effect of strong MHD activity on the time dependence of the lost triton flux for one of the discharges in Fig. 17 (37956). The average flux increases by about a factor of two above the level for discharges without MHD.

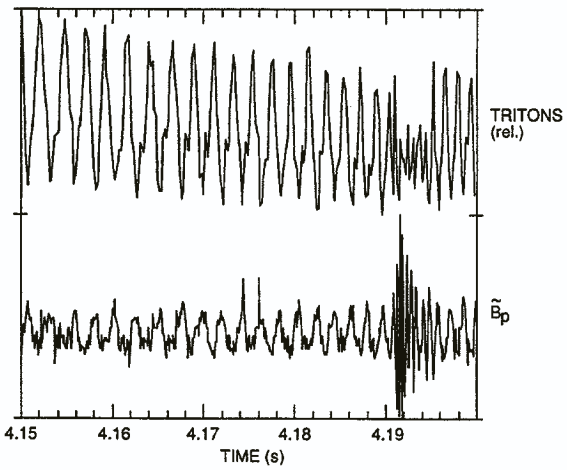

FIG. 26. Fast time-scale behaviour of the triton flux for the discharge shown in Fig. 25. The triton flux is clearly modulated at the same frequency as the MHD oscillations observed by a magnetic pickup coil at the plasma edge.

Although a detailed discussion of this phenomenon is beyond the scope of the present paper, one example of this MHD effect is shown in Figs 25 and 26. In this particular 1.6 MA discharge the net triton flux integrated over the whole discharge is increased by about a factor of two above the level of a similar discharge without MHD. In both figures the triton data come from the same PM channel as used for Fig. 17, which had a 20 kHz analog bandwidth and a sampling rate of 5 kHz in these cases.

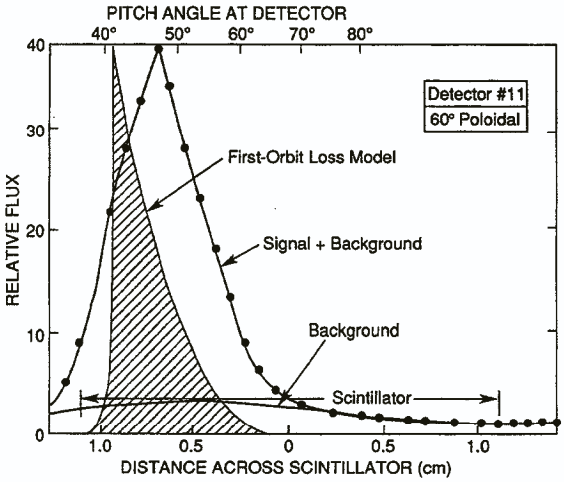

FIG. 27. Typical pitch angle dependence of the triton flux into detector No. 11 at ≈45° below the outer midplane (35323). The pitch angle peak is shifted with respect to that in detector No. 6 (Fig. 8), but it roughly agrees with the calculated first-orbit loss indicated by the shaded region. There is a ±5° uncertainty in the pitch angle calibration of the experimental data (not shown).

When the MHD frequency was below about 10 kHz (as in Fig. 26), the triton flux was clearly modulated with the MHD oscillations, with a maximum triton flux of up to ten times the triton loss level for the case without MHD. In many cases the MHD mode frequency decreased to near zero (mode 'locking') and then the triton flux remained anomalously high, as during the period from 4.25 s to 4.35 s in Fig. 25. When the MHD frequency was above about 20 kHz the modulations in the triton flux were not clearly visible (owing to the analog bandwidth of the PM circuit), but the triton flux was also increased above the level without MHD. Thus, some of the unusually high points obtained 'without MHD' in Fig. 17 may have been cases with either locked modes or high frequency modes which were not perceptible as modulations on the triton signal.

This effect of MHD activity on triton loss has been observed for several different types of coherent MHD modes, sawtooth crashes and fishbone-type oscillations. Further analysis of these phenomena is in progress.

3.12. Other poloidal detectors

Several other MeV ion detectors were installed during the 1988 TFTR run, as shown in Fig. 1. The poloidal array detectors No. 9 and No. 11 had relatively small signal levels because of their lower optical coupling efficiency (≈1/3 that of detector No. 6), but they were monitored regularly with the video camera in parallel with detector No. 6. Detector No. 4 was designed for 15 MeV protons and saw no signals, since there were few appropriate D–^{3}He discharges with ICRF heating. The four detectors of the toroidal array also had small signals because of inefficient optical coupling and were not regularly monitored.

Detectors No. 9 and No. 11 were positioned ≈60° and ≈45° below the outer equatorial plane, respectively. They had an aperture/scintillator geometry very similar to that of detector No. 6, except that the plane of the scintillator, apertures and box tops was aligned parallel to the local flux surfaces (see Fig. 1). Detector No. 11 had a 3 μm aluminium foil which passed tritons and protons in the same way as detector No. 6, but detector No. 9 had an 18 μm aluminium foil which passed only protons.

A typical pitch angle distribution from detector No. 11 is shown in Fig. 27 for a 1.2 MA discharge similar to that used for No. 6 in Fig. 8 (i.e. R = 245 cm, a = 80 cm, 16 MW NBI). The distribution is peaked at about 47°, i.e. at a significantly lower angle than for detector No. 6. However, the first-orbit loss code predicts that the critical angle should be about 42° for this detector location, and so this result is roughly con-

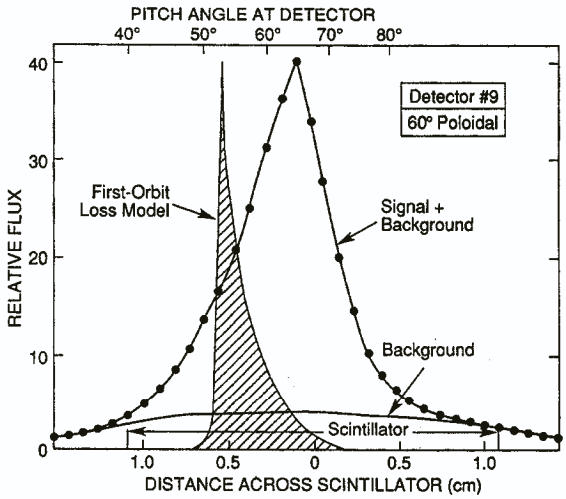

FIG. 28. Typical pitch angle dependence of the triton flux into the proton-only detector No. 9 at ≈60° below the outer midplane (35323). There appears to be a significant difference between the observed and the calculated pitch angle distributions for this detector, although the qualitative features of the proton loss are similar to the triton loss seen in detectors No. 6 and No. 11.

sistent with the code (given the ±5° systematic uncertainty in the pitch angle alignment). Other signatures of first-orbit loss observed in this detector are: (a) the gyroradius distribution for the detector was consistent with 1 MeV tritons (see Fig. 6); (b) the time dependence was similar to that of the neutron flux (as in Fig. 9); and (c) the flux decreased with plasma current (as in Fig. 13).

For the proton-only detector No. 9 the dependence of the signals on pitch angle, energy (i.e. gyroradius), time and plasma current had the same qualitative features as those seen in the triton/proton detectors No. 6 and No. 11. However, the peak in the pitch angle distribution was consistently in the 60–65° range, as shown in Fig. 28, which is significantly larger than the first-orbit code prediction of a 53° critical angle at this poloidal location. At present there is not explanation for this apparent discrepancy.

The ratio of the peak signal levels between detectors No. 6 and No. 11 was ≈1 ± 0.5 at 1.2 MA (after correction for the optical efficiency). This agrees fairly well with the expected ratio 1.3:1 obtained from the first-orbit code for these two detector locations. However, the ratio of the signals between detector No. 6 and detector No. 9 was also about 1:1 (after correction for optical efficiency), which, after also correcting for the estimated ratio of light flux for protons in detector No. 9 to tritons+protons in detector No. 6 (see Section 2.5), implies that the proton flux in detector No. 9 is about four times the triton flux in detector No. 6. This disagrees with the orbit code, which predicts that the flux at the position of detector No. 9 should be about 0.85 that of detector No. 6. Therefore, either there are losses other than first-orbit losses to detector No. 9 or the estimated triton/proton light output ratio of the scintillator is incorrect (this has not yet been measured experimentally).

The behaviour of these signals with varying major radius was also unexpected. The normalized flux in detector No. 9 *decreased* by about a factor of two between R = 245 cm and R = 238 cm, in contrast to the flux in detector No. 6, which *increased* by about a factor of two for the same change (Section 3.10). Also, the triton loss fraction in detector No. 11 decreased by more than a factor of four for the smaller plasmas; however, it is possible that the triton orbits were intercepted by a toroidal array detector downstream from detector No. 11 (see Fig. 1).

Improved measurements of the triton flux with poloidal angle are needed to resolve these points. Measurements near the midplane of TFTR are scheduled for 1990 [30].

4. CONCLUSIONS

In this paper we have described measurements of the loss of alpha-like MeV ions into detectors located at the bottom of the TFTR vessel. The results have been compared with the expected first-orbit loss due to the large banana widths of these ions at the plasma currents of 0.8–1.6 MA.

4.1. Summary of results

For escaping tritons measured ≈90° below the outer midplane, in discharges with normal minor radius without strong MHD activity, we note the following points:

(1) The pitch angle and energy distributions of lost tritons were consistent with the expected first-orbit loss, i.e. the loss was mainly at a pitch angle near 60°, corresponding to the fattest banana orbit, and at ≈1 MeV, corresponding to prompt loss at the birth energy;
(2) The time dependence of the triton loss followed the time dependence of the neutron (triton) source rate, as expected for prompt loss;
(3) The decrease in the lost triton fraction (i.e. lost triton flux normalized by the global triton creation rate) with increased plasma current was approximately consistent with the first-orbit model;
(4) The observed shift in peak of the pitch angle distribution with changing plasma current was approximately consistent with first-orbit model predictions, although the absolute value of the pitch angles was somewhat different from that calculated;
(5) The average triton loss fraction at a fixed plasma current was approximately constant over the whole range of TFTR D–D reaction rates, as expected from the first-orbit loss model for constant triton source and plasma current profiles;
(6) The observed scatter of about ±25% rms in the normalized lost triton flux at 1.6 MA could not be directly correlated with changes in plasma source or current profiles shapes;
(7) The triton loss fraction increased significantly for plasmas of small major radius, in a way not expected from the first-orbit loss model.

In addition:

(8) In discharges with strong MHD activity, the average triton loss fraction increased up to two to three times the level without MHD, these increases being

modulated in phase with the MHD mode for $f < 10$ kHz;

(9) The triton and proton loss observed in detectors located 45° and 60° below the outer midplane was qualitatively similar to that at 90°, as expected for first-orbit loss; however, the pitch angle distributions at these locations did not quite agree with the first-orbit code, and the estimated flux to the 60° proton-only detector was larger than expected.

4.2. Discussion of results

The general conclusion of these results is that the loss of alpha-like MeV ions as observed at the bottom of TFTR appears to be consistent with the expected first-orbit loss. Of course, it is not surprising that MeV ions are lost this way. The most interesting aspects of these results are the observation of some apparently 'anomalous' (non-first-orbit loss) effects, and also the apparent absence of some other potentially important non-first-orbit effects.

The most striking anomaly was the increased triton loss associated with strong coherent MHD (Sections 3.8 and 3.11). There are several possible causes for this: (a) modification of the triton source profile by MHD, such that regions of increased source periodically cross the triton trajectory, (b) magnetic 'ripple' induced loss of previously trapped tritons, due to low-n perturbations [11], and (c) leakage of previously confined passing tritons across the passing/trapped boundary, with the leakage being due to non-axisymmetric 'kicks' of the orbit by MHD [31]. Further clarification will require improved source profile measurements and more detailed theoretical modelling. Note that large MHD activity is expected in reactor grade plasmas near the high beta limit and/or if collective alpha instabilities are excited [32].

Another major anomaly was the factor-of-two larger than expected triton loss observed for small major radius plasmas in the bottom detector (Section 3.10), correlated with an unexpectedly small triton loss for the same plasmas in the 45° detector (Section 3.12). One plausible explanation could be that the triton source or the plasma current profiles are broader than presently calculated by SNAP for these smaller plasmas. Another possible explanation could be the presence of (unobserved) high frequency MHD activity in the smaller, lower q(a) plasmas.

A third, but less certain, anomaly concerns the unexpectedly large flux and the somewhat unexpected pitch angle distribution in the proton-only detector $\approx 60°$ below the outer equator. A possible cause for these effects is additional proton loss due to the TF field ripple. The theoretically predicted stochastic TF ripple diffusion process [6–8] causes the banana tips of confined trapped ions to randomly walk vertically, resulting in a loss which tends strongly towards the outer midplane region [9].

Preliminary results from the simplified RIPLOS code [11] predict a negligible stochastic TF ripple loss for normal TFTR plasmas; however, there are subtleties in more sophisticated treatments which require extremely large Monte Carlo computations. Unfortunately, there are at present no quantitative predictions for the poloidal and pitch angle distributions of this loss in TFTR, and so it is difficult to exclude possible TF ripple induced loss in the present results, particularly since global TF ripple losses tend to be relatively prompt (~ 10 ms loss time) and to decrease with increasing plasma current, similarly to prompt losses. Note that 'super-banana' loss due to ions trapped in the TF ripple wells could not be observed in the present detectors, since this loss occurs at pitch angles near 90° which are blocked in the present detector design.

Another theoretically predicted classical effect is the loss of partially thermalized MeV ions due to classical pitch angle scattering of confined ions born near the passing/trapped boundary [3, 33]. An early analytic estimate of this effect for alpha particles in a 1 MA TFTR plasma predicted a cumulative collisional loss fraction of $\approx 1\%$ for TFTR-like plasmas [3], which was approximately 10% of the first-orbit loss in that calculation. Since the predicted energy of these losses was mostly within about 20% of the birth energy, it would be difficult to exclude the presence of such an effect in the gyroradius distribution of Fig. 6, or the absence of delayed triton loss after NBI (since 20% triton energy loss occurs over about 0.2 s and since triton scattering is much slower than alpha scattering). More careful measurements are needed to check this effect, perhaps with a detector that has a better energy resolution.

A third potentially important effect, which was *not* observed in these experiments, was a large anomalous radial triton diffusion such as is observed for thermal ions in tokamaks. For the present experiment, such diffusion might be observable if confined passing tritons near the plasma centre moved radially outward, since they should eventually cross the passing/trapped boundary (if their magnetic moment is conserved) and so should be lost on the fattest banana orbits visible from our detectors. It is most likely that this apparently low MeV ion diffusion is due to the 'orbit averaging'

effect of large ion orbits in the presence of small-scale turbulence [11], as discussed in Ref. [34]. Other evidence for a relatively low diffusion rate for fast ions has been obtained for 100 keV NBI ions on TFTR [35] and for ICRF minority ions on JET [36].

In summary, the confinement of alpha-like MeV ions as measured with these escaping triton detectors in TFTR appears to be consistent with the simple first-orbit loss model, which implies that alpha confinement ought to be excellent in reactor grade plasmas, assuming that collective effects remain negligible. However, observations of enhanced triton loss during strong MHD activity and the possibility of enhanced losses near the (presently undiagnosed) outer midplane warrant further experimental and theoretical investigations.

4.3. Potential improvements

The present results are also limited in several respects, which suggests further improvements in experimental technique:

(1) Measurements should be made near the outer equatorial plane where the main TF ripple loss is expected [9] and where anomalous loss due to slow diffusion of confined orbits might also occur. Anomalous triton loss at the midplane could explain the anomalously low triton burnup often seen on TFTR [16]. A new outer midplane triton detector was recently installed on TFTR for this reason [30].

(2) The present measurements were all made with detectors located about 2 cm behind the limiter, which does not affect the collection of first-orbit loss (since these orbits move outward radially more than 2 cm in the toroidal direction between the limiter and the detector), but which may miss any slow radial diffusion of trapped tritons to the poloidal region of the detectors. The new midplane triton probe will be radially movable in order to explore this effect.

(3) Measurements of the triton and proton light outputs from these scintillators are needed in order to obtain an absolute calibration of these detectors. An absolute scintillator calibration is presently being made using a scintillator located inside a D–D generator.

(4) The spatial resolution of the present detector and camera imaging system is only marginally able to determine the shapes of the triton pitch angle and energy distributions; for example, the expected sharp cut-off at the critical pitch angle is not seen in the data of Fig. 8. Therefore, effects such as the source profile dependence of the pitch angle distribution and the possible presence of low energy triton components cannot be seen with the present system. Replacement of the coherent plastic fibre bundles by quartz fibres should increase the signal levels four times and so allow improved detector spatial resolution through reduced aperture sizes.

(5) Independent measurements of the plasma current and triton birth profiles are needed to resolve the effect of these profiles on triton loss. Input from the new multichannel neutron collimator should be very useful in this regard.

ACKNOWLEDGEMENTS

Thanks go to many people who contributed to this project. Help with the hardware came from G. Barnes, T. Deverell, D. Johnson, D. Manos, J. Montague, K. Owens, R. Pallidino, E. Tolnas and M. Ulrickson. Help with the data analysis codes came from C.W. Barnes, J. Felt, W. Heidbrink, J. Roberts, S. Scott and M. Zarnstorff. The magnetics data used for Fig. 21 came from M.E. Bell, and the magnetic fluctuation data for Figs 25 and 26 came from E.D. Fredrickson. Additionally, thanks are due to R. Duvall, H. Mynick, D. Sigmar and R. White for discussions of the theory, and to H. Furth, R. Goldston, L. Johnson, D. Meade and K. Young for their support for this project.

This work was supported by the United States Department of Energy, under Contract No. DE-AE02-76-CHO3073.

REFERENCES

[1] KOLESNICHENKO, Yu.I., Nucl. Fusion **20** (1980) 727.

[2] ANDERSON, D., HAMNÉN, H., LISAK, M., Thermonuclear Tokamak Plasmas in the Presence of Fusion Alpha Particles, Next European Torus, Rep. No. 91, EUR-FU/80/88-91 CEC, Brussels (1988).

[3] HIVELY, L.M., MILEY, G.H., Nucl. Fusion **20** (1980) 969.

[4] BITTONI, E., HAEGI, M., SANTINI, F., SEGRE, S.E., Nucl. Fusion **22** (1982) 1675.

[5] ANDERSON, D., BATISTONI, P., Nucl. Fusion **28** (1988) 2151.

[6] GOLDSTON, R., WHITE, R.B., BOOZER, A.H., Phys. Rev. Lett. **47** (1983) 647.

[7] TANI, K., TAKIZUKA, T., AZUMI, M., KISHIMOTO, H., Nucl. Fusion **23** (1983) 657.
[8] BELIKOV, V.S., KOLESNICHENKO, Yu.I., YAVORSKIJ, V.A., Fusion Technol. **15** (1989) 1365.
[9] GOLOBOROD'KO, V.Ya., YAVORSKIJ, V.A., Nucl. Fusion **29** (1989) 1025.
[10] MYNICK, H.E., DUVALL, R.E., Phys. Fluids B **1** (1989) 750.
[11] WHITE, R.B., MYNICK, H.E., Phys. Fluids B **1** (1989) 980.
[12] HEIDBRINK, W.W., CHRIEN, R.E., STRACHAN, J.D., Nucl. Fusion **23** (1983) 917.
[13] HEIDBRINK, W.W., HAY, R., STRACHAN, J.D., Phys. Rev. Lett. **53** (1984) 1905.
[14] BATISTONI, P., BITTONI, E., HAEGI, M., Nucl. Fusion **29** (1989) 673.
[15] CONROY, S., JARVIS, O.N., SADLER, G., HUXTABLE, G.B., Nucl. Fusion **28** (1989) 2127.
[16] STRACHAN, J.D., ZWEBEN, S.J., BARNES, C.W., et al., in Plasma Physics and Controlled Nuclear Fusion Research 1988 (Proc. 12th Int. Conf. Nice, 1988), Vol. 1, IAEA, Vienna (1989) 257.
[17] CHRIEN, R.E., KAITA, R., STRACHAN, J.D., Nucl. Fusion **23** (1983) 1399.
[18] HEIDBRINK, W.W., LOVBERG, J., STRACHAN, J.D., BELL, R.E., Nucl. Fusion **27** (1987) 129.
[19] BOSCH, H.-S., SCHUMACHER, U., in Controlled Fusion and Plasma Heating (Proc. 13th Eur. Conf. Schliersee, 1986), Vol. 10C, Part II, European Physical Society (1986) 124.
[20] MURPHY, T.D., STRACHAN, J.D., Nucl. Fusion **25** (1985) 383.
[21] STRACHAN, J.D., Nucl. Fusion **29** (1989) 163.
[22] MARTIN, G., JARVIS, O.N., KÄLLNE, J., Phys. Scr. **T16** (1987) 171.
[23] ZWEBEN, S.J., Phys. Scr. **T16** (1987) 119.
[24] ZWEBEN, S.J., Rev. Sci. Instrum. **60** (1989) 576.
[25] ZWEBEN, S.J., Nucl. Fusion **29** (1989) 825.
[26] SEGRE, E., Nuclei and Particles, Benjamin Press, Reading, MA (1977).
[27] HENDEL, H.W., PALLIDINO, R., BARNES, C.W., et al., In-situ Calibration of TFTR Neutron Detectors, Rep. PPPL-2679, Princeton Plasmas Physics Laboratory, Princeton, NJ (1990).
[28] PARK, H., BELL, M.G., GOLDSTON, R.J., et al., Energy Confinement Time and Electron Density Profile Shape in TFTR, Rep. PPPL-2651, Princeton Plasma Physics Laboratory, Princeton, NJ (1989).
[29] ZWEBEN, S.J., STRACHAN, J.D., BOIVIN, R.L., et al., in Controlled Fusion and Plasma Heating (Proc. 16th Eur. Conf. Venice, 1988), Vol. 13B, Part I, European Physical Society (1988) 39.
[30] BOIVIN, R.L., DUVALL, R.E., MYNICK, H., WHITE, R., ZWEBEN, S.J., Bull. Am. Phys. Soc. **34** (1989) 2014.
[31] DUVALL, R.E. (Princeton University), Topics in action-angle methods applied to tokamak transport and multiphoton excitation of atomic systems, PhD Thesis (1990).
[32] SIGMAR, D.J., HSU, C.T., WHITE, R.B., CHENG, C.Z., Alpha Particle Losses from Toroidicity Induced Alfvén Eigenmodes, Rep. PFC/JA8958, Plasma Fusion Center, Massachusetts Institute of Technology, Cambridge (1989).
[33] HSU, C.T., CATTO, P.J., SIGMAR, D.J., Phys. Fluids, B **2** (1990) 280.
[34] ZWEBEN, S.J., BOIVIN, R.J., DUVALL, R.E., et al., MeV ion confinement in the TFTR tokamak, to be published in Phys. Fluids, B.
[35] RADEZTSKY, R.H., SCOTT, S.D., KAITA, R., et al., in Controlled Fusion and Plasma Heating (Proc. 15th Eur. Conf. Dubrovnik, 1988), Vol. 12B, Part I, European Physical Society (1988) 79.
[36] START, D.F.H., BHATNAGAR, V.P., BOYD, D.A., et al., Confinement of MeV Ions in JET Created by Ion Cyclotron Resonance Heating, Rep. JET-P(89)84, JET Joint Undertaking, Abingdon, Oxfordshire (1989).

(Manuscript received 22 February 1990)